Article

High H₂ production in sediment-hosted hydrothermal fluids at an ultraslow spreading mid-ocean ridge

Check for updates

Alexander Diehl [1,2] ✉, Eirini Anagnostou [2,3], Patrick Monien [2], Thomas Pape [1,2], Eva-Maria Meckel [3], Miriam Römer [1,2], Leila Mezri [1,2], Wolfgang Bach [1,2], Donata Monien [4], Christian Hansen [2], Aaron Röhler [2], Katharina Streuff [1,2,5], Sabina Strmic Palinkas [6,7], Yann Marcon [1,2], Ines Barrenechea Angeles [7], Charlotte Kleint [1,2], Stig-Morten Knutsen[8] & Gerhard Bohrmann [1,2]

Hydrothermal systems at ultraslow-spreading mid-ocean ridges remain poorly characterized, particularly where sedimentary and ultramafic influences intersect. Here we present geochemical analyses of vent fluids collected in 2024 from the Jøtul hydrothermal field on the northern Knipovich Ridge. Major element concentrations, dissolved gases, and thermodynamic modeling are used to investigate fluid-rock interactions. The fluids exhibit exceptionally high CH_4 concentrations, that exceed those at the Guaymas Basin, and display characteristics typical of sediment-hosted hydrothermal systems, indicating thermal decomposition of organic matter in clastic sediments. In contrast, high H_2 (>15 mM) and low H_2S concentrations are more typical of ultramafic-hosted fluids, while geological evidence indicates that the vent field lies atop a detachment fault. Thermodynamic modeling suggests that these high H_2/H_2S ratios may result solely from degradation of organic matter followed by abiotic CH_4 oxidation at ~400 °C, rather than from reactions with ultramafic rocks. These results expand the known diversity of sediment-hosted vent fluid compositions and highlight fluid-sediment interaction as an underestimated source of carbon and hydrogen.

Hydrothermal venting in the ocean occurs along slow- to fast-spreading segments of the 60,000 km-long global system of mid-ocean ridges (MOR)[1]. Most spreading segments feature rocks of basaltic composition, and the chemistry of basalt-hosted vent fluids (cf [2–5].) has been shown to be primarily controlled by (1) reaction-zone depth and temperature[6,7], (2) the extent of water-rock interactions[5], and (3) phase separation of the seawater-derived fluids[8,9]. Hydrothermal processes along the 17,000 km-long ultraslow-spreading MOR are generally more varied and vent fluids exhibit a wider range of compositions[10]. With discontinuous divergence and alternating magmatic and tectonic accretion, the interplay between tectonics and magmatism results in the exhumation of ultramafic rocks[11]. Accordingly, hydrothermal fluids alternately interact with both mafic and ultramafic lithologies[12,13]. The variable influence of serpentinization reactions in ultramafic rocks, leads to variably H_2-enriched and Si- and H_2S-depleted

vent fluids as seen in the Lost City[14,15], Rainbow[16], Logatchev[17] and Kairei[12,13] vent fields. Similarly, MOR near continental margins are buried below terrestrial sediments, which affect hydrothermal vent fluid compositions. Syn-sedimentary volcanic activity interlayers basement rocks and sediments, causing diverse fluid compositions through alternating fluid-basement and fluid-sediment interactions[18–20]. In these settings gas composition in vent fluids is dominated by volcanic exhalation as shown in the Jade site[21,22] or controlled by thermal degradation of organic matter contained in sediments as suggested for the CLAM site[21,22]. Additionally, microbial processes in sediments can generate CH_4 and alter hydrocarbon composition to varying degrees, either when fluids heat up in the hydrothermal recharge zone or mix and cool in the discharge zone, as demonstrated in vent areas of the Okinawa Trough[23,24] and the Juan de Fuca Ridge[25]. Nevertheless, thermal degradation of sedimentary organic matter

[1]MARUM – Center for Marine Environmental Sciences, University of Bremen, Bremen, Germany. [2]Faculty of Geosciences, University of Bremen, Bremen, Germany. [3]Department of Physics and Earth Sciences, Constructor University Bremen, Bremen, Germany. [4]Leibniz-Centre for Tropical Marine Research (ZMT) GmbH, Bremen, Germany. [5]Department of Geography, Durham University, Lower Mountjoy, Durham, UK. [6]Department of Geosciences, UiT The Arctic University of Norway, Tromsø, Norway. [7]Department of Earth Science, University of Bergen, Bergen, Norway. [8]Norwegian Offshore Directorate, Harstad, Norway. ✉e-mail: diehl@uni-bremen.de

remains the dominant control on vent fluid compositions in many sediment-associated vent fields, such as Guaymas Basin[19,26], Escabana Trough[27], and Loki's Castle[28], where it also produces alkalinity through sulfate reduction[29]. Consequently, compared to basalt-hosted systems, vent fluids affected by sediment interactions typically exhibit lower metal contents, higher pH and alkalinity, as well as elevated concentrations of CO_2, CH_4, H_2 and other hydrocarbons. Their carbon isotope signatures and hydrocarbon ratios provide important constraints on the origin of these compounds in sediment-associated hydrothermal systems.

The 500 km-long Knipovich Ridge, as part of the Arctic Mid-Ocean Ridges[30], extends from the Molloy Fracture Zone in the north to the Mohns Ridge in the south (Fig. 1a). It represents a unique geological setting, where ultraslow spreading coincides with proximity to the continental margin and terrestrial sediment deposition. Spreading initiated during the opening of the Fram Strait[31,32] around 20 Ma ago and occurs in an ultraslow, asymmetric, oblique mode. Spreading rates decrease from 15.1 to 14.0 mm yr^{-1} northward as asymmetry increases. Here, divergence is highly oblique, with an angle of 40–53° between the ridge and the spreading direction, leading to

a reduced spreading rate perpendicular to the ridge axis[33]. Teleseismic data and ocean bottom seismometers[34,35] indicate that magmatic activity is concentrated in magmatically robust zones like the Logachev Volcanic Center (the most prominent volcanic center along the Knipovich Ridge[36]), which are interspersed with magmatically starved sections characterized by deeper hypocenters and aseismic behavior. While detachment faulting has not been documented along most of the Knipovich Ridge[35,37], it dominates in the north, where magma supply and spreading rates are lowest[37].

The Jøtul hydrothermal field at the northern Knipovich Ridge was discovered in 2022 during the research expedition with *R/V MARIA S. MERIAN* (MSM109[38]) and is situated east of the Brøgger Axial Volcanic Ridge (AVR, Fig. 1b). Located ~5 km from the ridge axis, it sits amidst numerous normal faults[39] on a sediment-covered neovolcanic high at the eastern boundary of the rift graben. Sediments along the Knipovich Ridge consist of a mixture of transported terrigenous and pelagic components and contain higher amounts of organic matter. Surface sediment samples collected on the central Knipovich Ridge ~45 km south of the Jøtul hydrothermal field show concentrations of total organic carbon (TOC) of
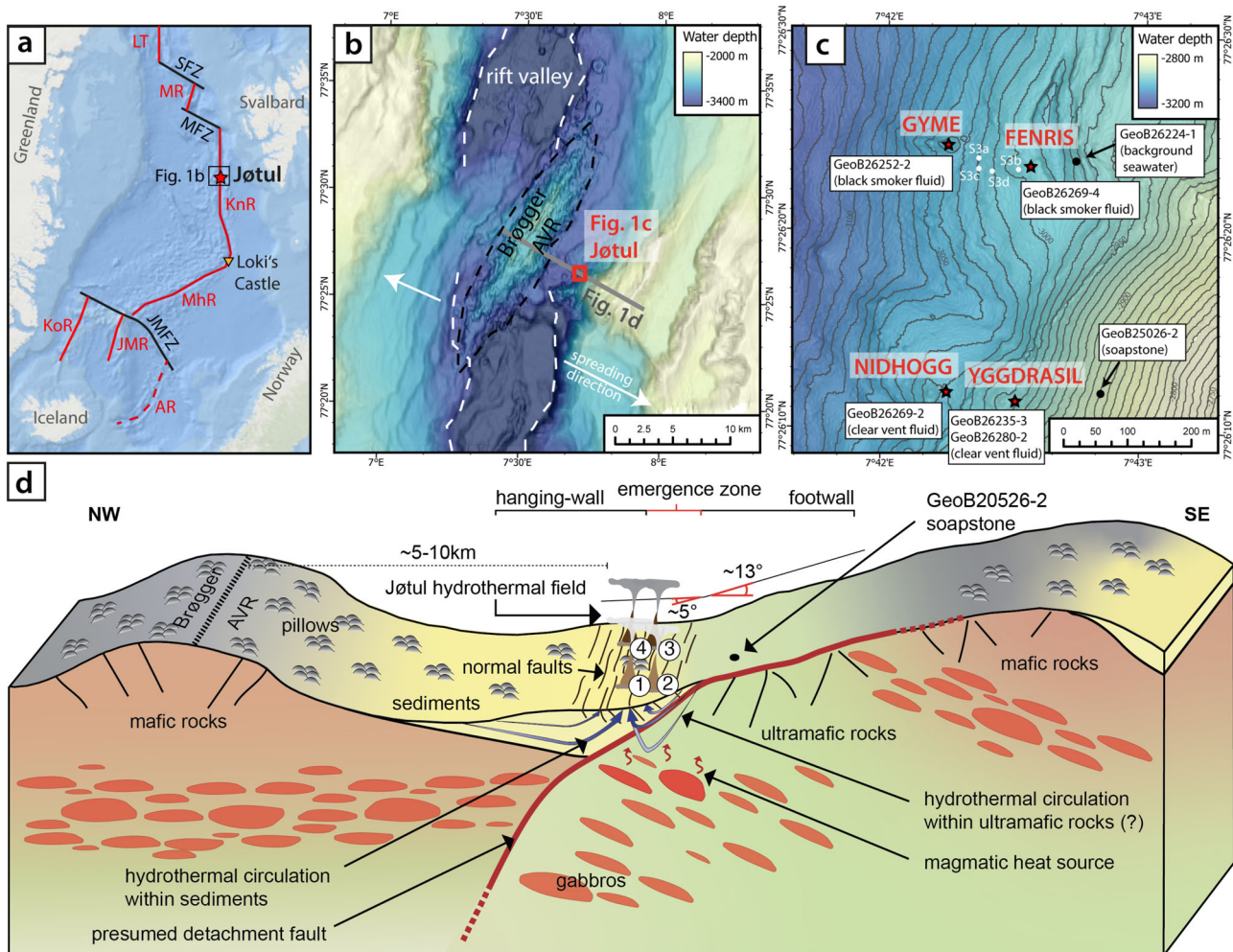

Fig. 1 | Location and geological setting of the Jøtul hydrothermal field. a Overview of the Norwegian-Greenland Sea (Esri GEBCO basemap) with main ridge segments (red lines, dashed line: inactive) and transform faults (black lines). AR Aegir Ridge, JMFZ Jan Mayen Fracture Zone, JMR Jan Mayen Ridge, LT Lena Trough, KnR Knipovich Ridge, KoR Kolbeinsey Ridge, MhR Mohns Ridge, MR Molloy Ridge, MFZ Molloy Fracture Zone, SFZ Spitsbergen Fracture Zone. **b** Location of Jøtul hydrothermal field at the eastern flank of the rift valley close to the Brøgger AVR (Axial Volcanic Ridge). Ship-based multibeam bathymetry aquired during cruise MSM109[46]. Dashed white and black lines mark the boundaries of the rift valley floor and the Brøgger AVR, respectively. **c** High-resolution (AUV-derived[46]) bathymetry map of the fluid sampling sites in the Jøtul hydrothermal field (red stars), seafloor observations (white dots, S3a-S3d) and soapstone sample (black dot, GeoB20526-2). Maps in this figure were created using ArcGIS® software by Esri. **d** Conceptual schematic profile of the tectonic, lithological and hydrothermal framework below the Jøtul hydrothermal field. The sampled vents are enumerated as following: (1) Nidhogg and (2) Yggdrasil, (3) Fenris, and (4) Gyme. The black dot shows the location of soapstone GeoB25026-2 (metasomatized peridotite, c.f. **c** Given slopes represent averaged seafloor slopes measured from the bottom of the rift valley floor to the vent site (5°) and from the vent site to near the ridge crest in the east (13°).

0.2–1 wt.%[40] and it was suggested that the organic matter in these sediments originated from coastal areas around Svalbard. Sediments from western Svalbard fjords (Kongsfjorden, Adventfjorden, Hornsund) have high contents of both biogenic and terrestrial components and contain 1.1–2.1 wt.% TOC[41]. However, due to the proximity of the Jøtul field to the limits of the Eurasian ice sheets during the last glacial period[42], its location near the present maximum sea ice extent[43], and the predominant south-to-north flow direction of the West Spitsbergen Current[44], the mentioned fjords may not represent the exclusive source regions of the sedimentary organic matter.

Hydrothermal activity at the Jøtul hydrothermal field includes two black smokers, named Fenris and Gyme[45] (Fig. 1c, Supplementary Table S1, Supplementary Fig. S2a–d), and two structures releasing clear, shimmering fluids from flanges and fissures, named Yggdrasil and Nidhogg[46] (Supplementary Table S1, Supplementary Fig. S2e–h). All of them are hosted in larger sulfide mounds that crop out of the surrounding sediments (Supplementary Fig. S3a–b) and have been subject to a certain degree of mass wasting (Supplementary Fig. S3c). Sporadically exposed pillow basalts near the vent field (Supplementary Fig. S3d) suggest locally thin sediment cover or syn-sedimentary volcanic activity.

At the location of the vent field the seafloor slope is dipping westwards and changes from dipping ~5° west of the vent field, to ~13° east of the vent field (Fig. 1d). This seafloor morphology may indicate emplacement of the vent field adjacent to the emergence zone of a westward-dipping detachment fault, which bounds the rift graben in the west and a NE-SW striking ridge east of the vent field. Indeed, such a change in seafloor slope may be typical for detachment faulting and mark the transition between the hanging wall cutoff and the corrugated surface of the exposed footwall[47]. The western flank of the ridge in the east is interpreted to represent the uplifted footwall of this westward-dipping detachment fault (Fig. 1d). Samples of soapstone (Supplemenary Fig. S4, Supplementary Table S5) recovered only 100 m east of Yggdrasil[38] support this interpretation (Fig. 1c, d). Soapstones are silica-metasomatized ultramafic rocks, and high Ni and Cr concentrations in the bulk rock analyses (Supplementary Table S5) indicate that the precursor rock was probably a mantle peridotite. Both, a low-angle seafloor slope and occurrence of (altered) ultramafic rocks have mainly been described along detachment footwalls[48,49] and are supported by geodynamic numerical models that involve mixed tectonic and magmatic accretion[50–52].

During expedition MSM109 in 2022 fluid samples were collected for the first time from hydrothermal vents in the Jøtul field[46]. However, the fluid samplers (KIPS; Kiel Pumping System) used were not gas-tight, so the concentrations of dissolved gases represent minimum values. Exceptionally high CH_4 concentrations of up to 5 µM in the non-buoyant plume above the vent field[46] suggested even higher CH_4 concentrations in the vent fluids than reported previously. During expedition MSM131[45] in 2024, isobaric gas-tight (IGT) fluid samplers[53] were used to re-sample the hydrothermal vents at the Jøtul field. The recently aquired fluid samples have higher CH_4 concentrations and are less diluted with seawater. In this publication, we report concentrations of dissolved volatiles, major fluid compositions, and stable isotope ratios from these gas-tight vent fluid samples and discuss the subsurface processes driving the formation of these particularly volatile-rich fluids.

Results and discussion
Vent fluid compositions and hydrothermal endmember
The hydrothermal fluids sampled (Supplementary Table S6, Supplementary Table S7) vented with temperatures of 214–314 °C (Fig. 2a). Low Mg and SO_4 concentrations (<4.1 mM and <2.9 mM) indicate that seawater entrained during sampling was minor and that endmember hydrothermal fluids are essentially free of Mg and SO_4. Vent fluid endmembers (Table 1) were calculated using a mass balance two-component mixing model, assuming a Mg-free hydrothermal endmember fluid as experimentally determined[54]. Since the samples were vent fluid-dominated, the measured and calculated compositions closely match. Endmember temperatures were derived using isenthalpic-isobaric mixing models (Supplementary Fig. S8)

based on thermodynamic data of the H_2O-NaCl system[55]. These temperatures slightly exceed measured temperatures, ranging from 223 °C at Nidhogg to 297–318 °C at the other three vents. The fluid compositions are typical of sediment-hosted hydrothermal systems, having elevated pH (Fig. 2b), alkalinity (3.5–4.6 mM) and NH_4^+ concentrations (1.7–5.3 mM) and low metal contents (Fe: <33 µM, Mn: <0.21 mM) compared to basalt-hosted systems. Noticeably, CH_4 concentrations (49.7–66.3 mM) are the highest ever reported for mid-ocean ridge hydrothermal fluids (Fig. 2c) and with CO_2 concentrations of 36.0–41.6 mM both values far exceed those from the diluted, and partly degassed KIPS samples recovered in 2022[46].

The $\delta^{13}C$ values of CH_4 (–32.3 to –31.9‰) closely match extrapolated endmembers from samples recovered in 2022, while $\delta^{13}C$-CO_2 values (–11.7 to –10.7‰) and δ^2H-H_2 values (–425.2 to –372.9‰) from the Jøtul fluids are reported for the first time. These carbon isotope ratios along with molecular compositions of light hydrocarbons ($C_1/(C_2–C_3)$) provide insights into carbon sources in hydrothermal fluids, distinguishing between abiotic, thermogenic, and biogenic origins[24]. The $\delta^{13}C$ values of CO_2 and CH_4, combined with a $C_1/(C_2–C_3)$ value of ~108, indicate a mix of abiotic reactions and thermogenic degradation of organic matter with minor biogenic contribution that would typically be indicated by higher $C_1/(C_2–C_3)$ values[24,25]. The $\delta^{13}C$-CO_2 values are lower than in basalt-hosted hydrothermal systems, which average at –5.74 ± 3.5‰, (MARHYS DB 4.0; Mg <5 mmol kg^{-1}) and reflect a primitive mantle degassing signature. Fluids from the Middle Valley vent site have lower values between –33.9 and –20.7‰[25], suggesting a substantial contribution from thermogenic processes. The $\delta^{13}C$-CO_2 values at Jøtul are similar to those at Loki's castle and we accordingly interpret dissolved CO_2 to have a mixed magmatic and thermogenic origin[28].

Elevated Sr (>142 µM) and radiogenic Sr isotope ratios (0.7085–0.7091)[46] point to terrestrial material mobilization[20,26,56]. Chlorinity is 8–14% lower than seawater (Fig. 2d), and along with high water stable isotope ratios (δ^2H-H_2O and $\delta^{18}O$-H_2O of +3.0–4.0‰ and +1.9–2.5‰, respectively), suggests subsurface phase separation under supercritical conditions, rather than dehydration reactions of low δ^2H detrital clays[57]. Silica concentrations (10.6–14.0 mM) align with endmember concentrations from cruise MSM109 and are below quartz saturation for seafloor pressure and venting temperatures. Hydrogen endmember concentrations (14.8–19.1 mM) are approximately twice as high as those previously reported for sediment-hosted hydrothermal vent fluids[58,59]. These concentrations resemble those typical of ultramafic-hosted systems such as the Rainbow[16] or Logatchev[17] vent fields (Fig. 2e). Coinciding with these high H_2 concentrations, are concentrations of H_2S (0.9–2.5 mM), which are lower than those reported for most sediment-hosted sites elsewhere (Fig. 2f). The high H_2/H_2S ratios of Jøtul vent fluids are similar to what has been reported for fluids from ultramafic-hosted vents. The Jøtul vent fluids are particularly enriched in dissolved carbon species and have higher H_2 concentrations than reported in other studies of sediment-hosted vent fluids. This could point to the presence of ultramafic rocks in the reaction-zone of the hydrothermal system, which could be accountable for the observed high H_2 and low H_2S concentrations by magnetite-bornite-chalcocite-fluid equilibria[60] or pentlandite desulfurization reactions[61]. The geological observation of altered ultramafic rocks and situation over an inferred detachment fault supports the notion that the fluids interact with ultramafic rocks along their flow paths.

Subsurface conditions at the Jøtul field
Isotope equilibrium temperatures were calculated for δ^2H (H_2O-H_2 and CH_4-H_2 exchange) and $\delta^{13}C$ (CH_4-CO_2 exchange)[62]. While Nidhogg exhibited lower δ^2H equilibrium temperatures between 277 and 281 °C (Supplementary Fig. S9a, b), temperatures across the other vents ranged from 333 to 346 °C. $\delta^{13}C$ equilibrium temperatures of 350–360 °C (Supplementary Fig. S9c) are slightly higher due to slower isotope exchange kinetics despite elevated temperatures (the isotope exchange slows down upon cooling). The close agreement between $\delta^{13}C$ and δ^2H equilibrium
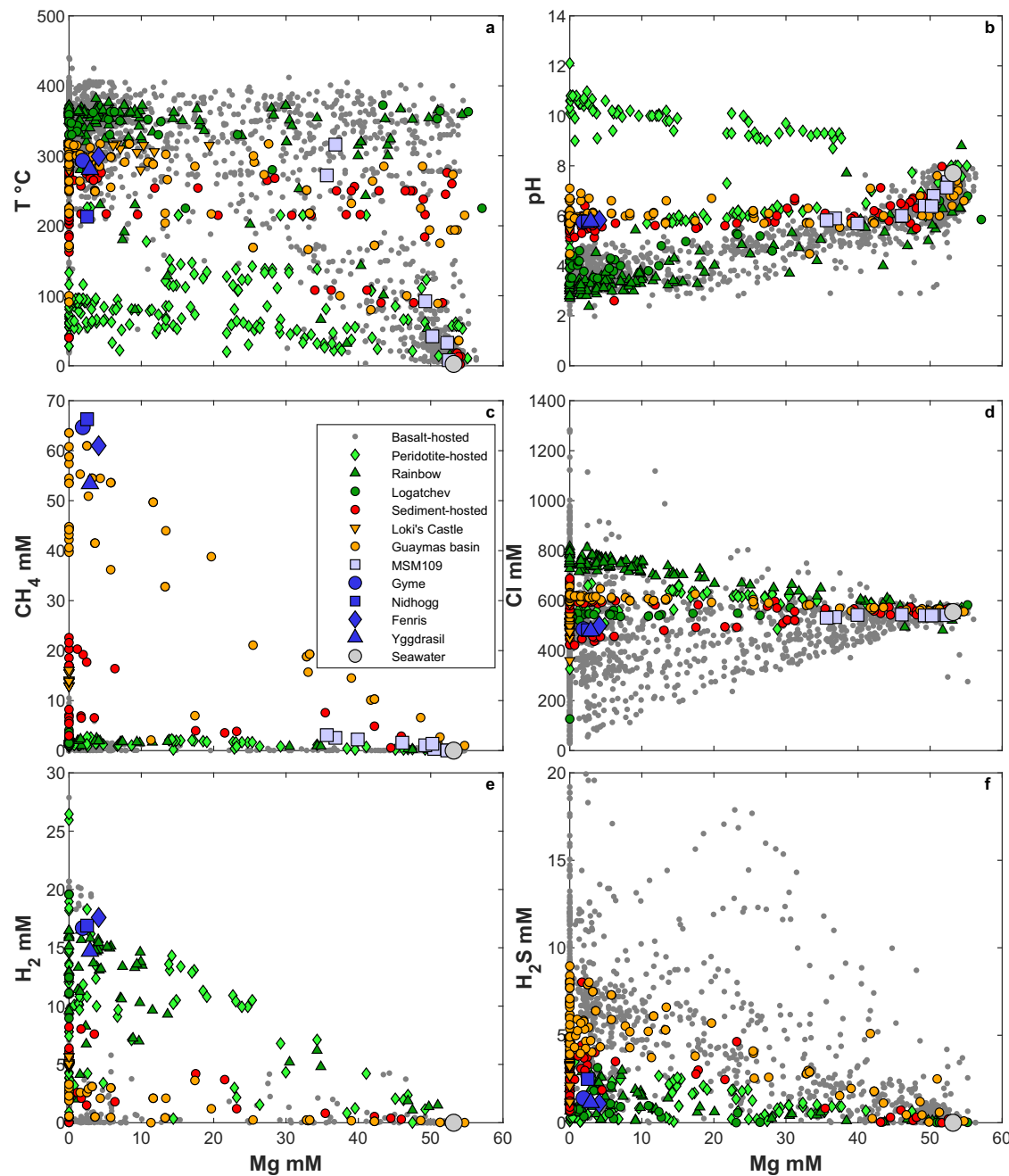
Fig. 2 | Vent fluid data from samples of the Jøtul hydrothermal field in the context of mid-ocean ridge hydrothermal fluids. a−f Mg concentrations vs temperature, pH, CH_4, Cl, H_2 and H_2S. Most chemical parameters for the Jøtul fluids plot in the typical range of sediment-hosted vent fluids (pH, CH_4), while others plot in the range rather typical of ultramafic-hosted (mostly peridotite) vent fluids (H_2S, H_2).

Compositions of Loki's Castle and Guaymas Basin vent fluids (sediment-hosted) are highlighted in orange. Compositions of Rainbow and Logatchev vent fluids (ultramafic-hosted) are denoted in dark green. Data for comparison is from MARHYS database[58,59].

temperatures (within 10–20 °C) and the overall similar vent fluid compositions support a common reaction-zone for all vent fluids. However, the lower δ²H equilibrium temperatures at Nidhogg suggest conductive cooling before venting that might be related to a subtle depletion of CO_2, NH_4, and alkalinity, as well as a subtle enrichment in CH_4 and H_2S compared to the other three Jøtul vents.

The concentrations of CH_4, CO_2 and H_2 can be related by the Sabatier reaction:

$$2H_2O + CH_4 \rightleftharpoons CO_2 + 4H_2 \qquad (1)$$
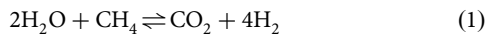
The corresponding mass action equation can be solved for H_2 concentrations from measured CH_4/CO_2 ratios and the temperature-dependent equilibrium constants. Concentrations of H_2 and CH_4/CO_2 ratios can thus be used to calculate chemical equilibrium temperatures. These calculated temperatures for the Sabatier reaction equilibrium are 386 to 391 °C and higher than isotope equilibrium temperatures for all vent fluids (Supplementary Fig. S9d).

At isotopic equilibrium temperatures the reaction would yield only 5–8 mM H_2, which is notably lower than the measured concentration (15–18 mM) and indicates isotopic exchange during fluid ascent and cooling, as observed in the Middle Valley vent field, Juan de Fuca Ridge[25].

Table 1 | Calculated zero-Mg endmember compositions for isobaric-gas-tight fluid samples from individual orifices in the Jøtul hydrothermal field

GeoB#	Vent-ID	T_{EM} °C	pH$_{in\text{-}situ}$	B mM	Ba µM	Ca mM	Fe µM	K mM	Li mM	Mg mM	Mn mM	Na mM
26252-3	Gyme	302	6.8	2.50	38	35.8	34	22.7	1.53	0	0.19	374
26269-2	Nidhogg	223	6.4	2.47	19	35.2	13	21.9	1.47	0	0.19	368
26269-4	Fenris	319	7.1	2.59	5	37.0	30	22.8	1.54	0	0.23	380
26235-3 & 26280-2	Yggdrasil	299	6.9	2.45	15	35.4	25	21.6	1.46	0	0.20	361
-	**Average EM Jøtul**	**286**	**6.8**	**2.50**	**19**	**35.9**	**25.6**	**22.3**	**1.50**	**0**	**0.20**	**371**
-	Average EM Guaymas	259	-	1.64	22	32.1	44.4	44.2	0.96	0	0.15	503
-	Average EM Loki	307	-	2.03	29	28.8	26.9	35.0	1.95	0	0.07	397
	Average EM Logatchev	315	-	0.34	25	28.7	2150	23.2	0.24	0	0.34	405
	Average EM Rainbow	348	-	0.25	74	70.0	23700	20.0	0.35	0	2.03	579

GeoB#	Vent-ID	NH$_4$ mM	Si mM	Sr µM	Br µM	Cl mM	SO$_4$ mM	PO$_4$ µM	NO$_3$ µM	CO$_2$ mm	CH$_4$ mM	H$_2$ mM	H$_2$S mM
26252-3	Gyme	5.5	13.6	157	797	484	1.0	1.1	5.0	41.9	67.1	17.3	1.5
26269-2	Nidhogg	1.8	11.1	155	782	479	0.9	0.7	2.9	37.7	69.6	17.7	2.6
26269-4	Fenris	3.0	15.2	156	823	495	0.8	0.7	2.6	44.9	66.1	19.1	1.2
26235-3 & 26280-2	Yggdrasil	2.9	13.0	151	778	475	1.1	2.0	4.5	41.4	56.5	15.6	1.2
-	**Average EM Jøtul**	**3.3**	**13.9**	**155**	**795**	**483**	**0.9**	**1.1**	**3.8**	**41.5**	**64.8**	**17.4**	**1.6**
-	Average EM Guaymas	14.2	12.5	216	1060	617	0	-	-	44.1	50.6	1.7	6.9
-	Average EM Loki	5.4	15.2	111	652	505	5.3	-	-	24.3	14.2	5.1	3.8
-	Average EM Logatchev	--	9.1	121	770	496	2.0	-	-	4.8	2.3	11.9	1.7
-	Average EM Rainbow	0.002	7.1	195	1198	774	0	-	-	19.4	1.9	14.1	2.0

The composition of the Yggdrasil endmember was calculated by averaging two vent fluid samples. The average Jøtul hydrothermal endmember is given in bold font and compared with compositions of other sediment- and ultramafic-hosted vent sites (Guaymas Basin, Loki's Castle, Rainbow, Logatchev). Compositions for these vent sites were derived by averaging all respective endmember fluids in the MARHYS database 4.0[58].

GeoB#: Sample identifier; EM endmember, mM mmol·l^{-1}, µM µmol·l^{-1}, mm, mmol·kg^{-1}. Endmember temperatures (T_{EM}) for Jøtul fluids were calculated via isenthalpic-isobaric mixing (S8) using seafloor pressure (300 bar) and a seawater temperature of 2.2 °C. In-situ pH values were derived via chemical speciation calculation for endmember temperatures/compositions.

Chemical equilibrium, which can be reached up to 100 times faster[63,64], is likely more reliable for assessing reaction-zone temperature than isotopic equilibrium. Some studies suggested that in most sediment-free hydrothermal vent fluids the Sabatier reaction is not a favorable process to explain CH$_4$ concentrations[65] and that hydrothermal conditions may prevent Sabatier equilibrium from establishing itself[66,67]. But other studies indicate rapid kinetics depending on reaction direction, particularly when excess CH$_4$ drives H$_2$ and CO$_2$ production[25,68].

Chlorine concentrations and water stable isotopes (δ^2H-H$_2$O, δ^{18}O-H$_2$O) suggest phase separation in the subsurface. Given a water depth of 2953–3021 mbsl (meter below sealevel) and in-situ pressures of 294–301 bar, phase-separated fluids with temperatures below 320 °C have been affected by substantial conductive cooling. The seafloor pressure at the Jøtul field corresponds to the critical point of seawater at 403–406 °C[69], which marks the minimum temperature for phase separation. Silica endmember concentrations (13–15 mM) are below quartz saturation at seafloor pressure and temperature of venting. However, assuming a temperature of 386–392 °C calculated for the Sabatier reaction equilibrium, the most silica-rich fluid (15.1 mM Si; Fenris) corresponds to silica saturation at 330 bar (Fig. 3). A phase-separated fluid with a chlorinity of 500 mM at this depth has an equilibrium temperature of 420 °C. The Si-Cl thermobarometer, commonly used to estimate reaction-zone depth, would suggest 480–500 °C

at 495–545 bar (Fig. 3). However, high temperatures during phase separation likely prevent fluids from retaining this equilibrium signature during ascent along pressure-temperature paths that come with lower Si solubilities. We estimate that the reaction-zone occurs at pressures below 360 bar (<600 mbsf; meter below seafloor), with temperatures between the Sabatier equilibrium (386 °C) and vapor-brine equilibrium (420 °C). These conditions explain observed CH$_4$, CO$_2$, and H$_2$ concentrations via Reaction (1) and Si and Cl levels through solubility and phase separation constraints.

Constraints on the shallow depth of the reaction-zone have important implications for the nature of the heat source driving hydrothermal circulation in the Jøtul field. In general, hydrothermal circulation can be driven not only by magmatic heat but also by heat released during the exhumation of hot mantle rocks along detachment faults. In many nearly amagmatic detachment faults traces of hydrothermal circulation have been detected at greater depths of up to ~15 kmbsf[70,71], but chemical data from the vent fluids indicating a shallow reaction-zone suggest that this is likely not the case for the Jøtul field. We therefore assume that hydrothermal circulation at Jøtul is driven by a magmatic heat source within the detachment footwall. Such footwall intrusions are not uncommon and have been proposed in several oceanic core complexes[47,72–74]. The hydrothermal reaction-zone above a magmatically driven hydrothermal system is typically separated from the magma by a conductive boundary layer (CBL)[75]. The thickness of the CBL

Fig. 3 | Reaction-zone depth estimate for Jøtul vent fluids. Black lines denote quartz saturation as a function of pressure and temperature and show Si-isopleths of 13, 14 and 15 mM Si. The blue line shows the pressure-temperature relation of a phase-separated low salinity fluid (3.1 wt.% NaCl) with a conjugate brine of variable composition. Red patches mark the conditions of the hydrothermal reaction-zone inferred by a) the Sabatier equilibrium temperature, Si-solubility and phase separation constraints and (b) the Si-Cl thermobarometer.
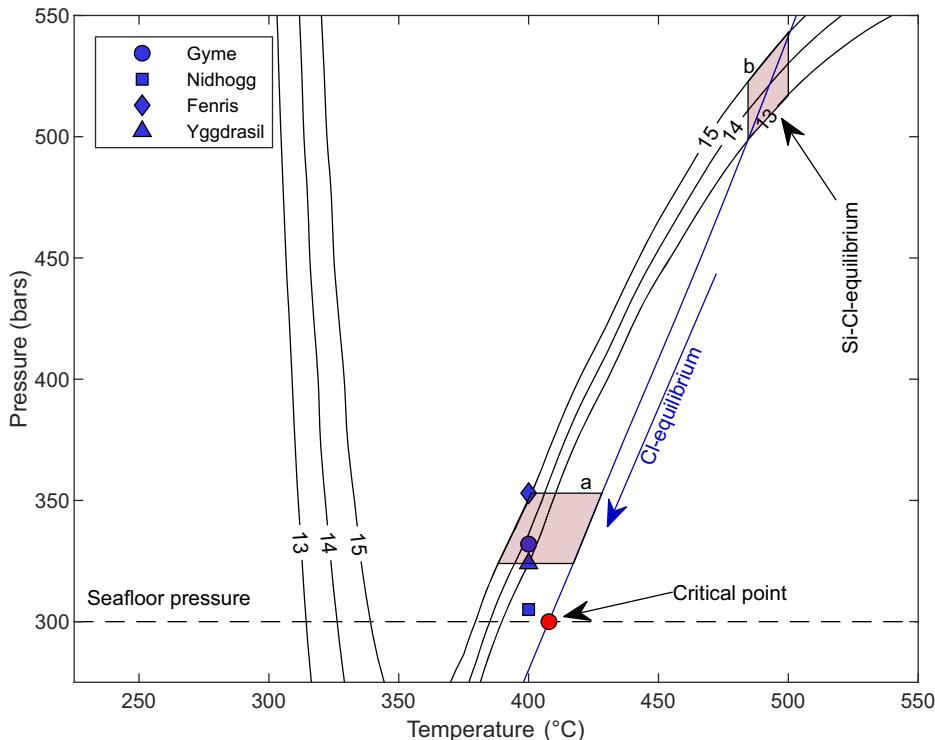
ranges from a few tens to a few hundreds of meters and depends on the current magma supply rate as well as on the permeability of the layer itself[75,76]. Hence the magmatic heat source can be expected to occur only slightly deeper than the estimated reaction-zone depth of ~300–2500 mbsf (corresponding to a pressure of 330–545 bar). Our interpretation is supported by the occurrence of fresh pillow lavas cropping out of the sediments near the vents, which indicates geologically recent volcanic activity. Furthermore, the mixed magmatic and thermogenic origin of CO_2 suggested by $\delta^{13}C$ ratios in the vent fluids supports this assumption.

H_2 production from alteration of ultramafic rocks
The high H_2 and low H_2S concentrations in the Jøtul fluids are atypical for basalt- or sediment-fluid interactions but consistent with ultramafic-hosted vent sites. The high H_2/H_2S ratios can be explained by buffering of the fluid composition by a pentlandite-pyrrhotite-heazlewoodite mineral assemblage[61] at 350 bar and 400–425 °C (Fig. 4). Supporting an ultramafic origin of these concentrations, mineral-buffered experiments reacting seawater with hematite-magnetite or pyrite-pyrrhotite-bearing sedimentary material produced only ~4 mM H_2[77]. Hydrothermal experiments with organic-rich diatomaceous ooze at 400 °C and 400 bar yielded <7 mM H_2 and relatively high H_2S concentrations (>3 mM)[68]. We employed thermodynamic reaction path models that confirm the results of these experimental investigations and the range of concentrations for vent fluid compositions associated with circulation through sediments. When seawater reacts with sulfide-bearing sediments (e.g., pyrite-pyrrhotite), H_2S concentrations are expected to be above 5 mM. Similarly, in sulfide-free sediments reduction of seawater sulfate produces high H_2S concentrations of >5 mM at temperatures around 400 °C. The observed high H_2/H_2S appears inconsistent with a pure sediment control of vent fluid composition and could support the idea that ultramafic rocks are present in the hydrothermal root zone below the Jøtul field.

### H_2 production through thermal degradation of organic matter
We conducted thermodynamic reaction path calculations to examine if sediment-fluid interaction may also account for high H_2/H_2S ratios under specific conditions. In our model we react sulfate-poor seawater with

organic matter-bearing sediment (Fig. 5, Supplementary Table S10, Supplementary Fig. S11). Such a fluid can be expected to form in the recharge zone of hydrothermal systems due to anhydrite precipitation[2,6]. At intermediate temperatures (150–200 °C) seawater is depleted in SO_4, as anhydrite precipitation occurs rapidly, while thermogenic SO_4 reduction is negligible. Organic matter is represented in the model by S- and N-bearing amino acids (cysteine, alanine) and alkane (propane) that act as sources of C-, S- and N-species for the vent fluids. In the model we used a concentration of 0.22 wt.% of total organic matter, which represents a conservative estimate at the lower spectrum of measured TOC concentrations (0.2−1 wt.%)[40] in surface sediments along the Knipovich Ridge, 45 km south of the vent field. The carbon oxidation state in the organic matter controls the CH_4/CO_2 ratio and Reaction (1) produces H_2 equilibrium concentrations over large ranges of water-to-rock ratios, while CH_4, CO_2, H_2S, and NH_3 increase with decreasing water-to-rock ratios, due to progressive fluid-sediment interaction and associated element uptake of sedimentary organic matter. Our model calculations indicate that if a SO_4-poor fluid enters the high-temperature reaction-zone, thermal degradation of organic matter may result in high H_2/H_2S ratios. This model successfully explains concentrations of C-, H-, N- and S-species in the hydrothermal endmember fluids and suggests the reaction with ultramafic rocks are not required to explain the Jøtul fluid composition.

Summary and conclusions
The Jøtul hydrothermal vent fluids were sampled at higher temperatures and were more volatile-rich in 2024 than those collected in 2022 (MSM109). They are characterized by elevated pH, NH_4^+ and alkalinity, along with low metal concentrations. These characteristics are features typical of sediment-hosted hydrothermal vent fluids compared to those hosted in basalt. Additionally, the fluids carry high concentrations of CH_4, CO_2 and H_2 and low H_2S concentrations. High H_2/H_2S ratios are rather untypical for sediment-associated vent fluids and the geological setting around the vent field with probable detachment faulting and occurrence of ultramafic rocks give rise to the possibility of hybrid vent fluid compositions derived from both fluid-rock interactions with ultramafic rocks and sediments. Although water-ultramafic rock interaction cannot be entirely ruled out,

Fig. 4 | H₂S vs H₂ concentrations in hydrothermal vent fluids hosted in different rock types in comparison with the Jøtul fluids. The lines show H_2/H_2S ratios as produced by different rock buffers at 350 bar and temperatures denoted in the legend. "po-py: pyrrhotite-pyrite buffer (Eq. 5); "pn-hz": pentlandite-pyrrhotite-heazlewoodite buffer (Eq. 6). Compositions of Loki's Castle and Guaymas Basin (sediment-hosted), as well as, Rainbow and Logatchev (ultramafic-hosted) vent fluids are highlighted.
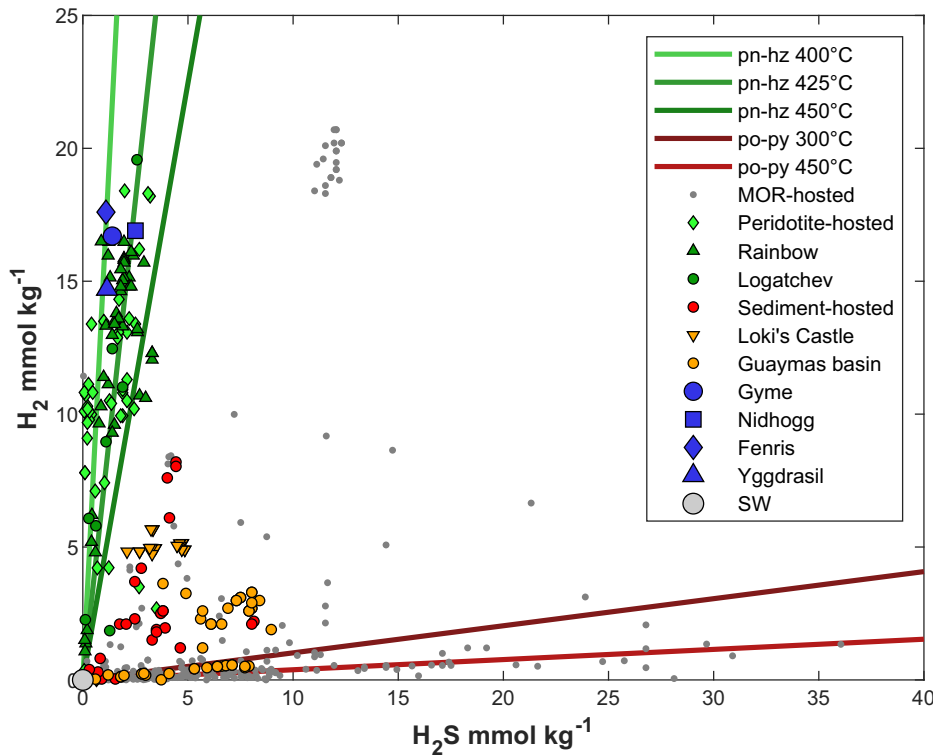
concentrations of H_2 and H_2S are readily explained by SO_4 reduction and CH_4 oxidation following thermal degradation of organic matter in a shallow reaction-zone involving only sediments and temperatures around 400 °C. Despite being shallow in the subseafloor, the reaction-zone, due to the great water depth (~3000 mbsl), likely occurs at higher pressure and temperature than other sediment-associated vent sites like Minami-Ensei[20,24] (~720 mbsl), Iheya North[23,78] (~1000 mbsl) and CLAM Site[22,29] (~1400 mbsl) in back-arc basins, or like Guaymas Basin[19] (~2000 mbsl) and Loki's Castle[28] (~2400 mbsl) in mid-oceanic ridges. The higher pressure and temperature lead to the highest H_2 concentration in such a sediment-associated vent site measured so far. Our results challenge the general view of high H_2 concentrations as an indicator for water-rock reactions with ultramafic rocks and suggest that sediment-associated vent fluids are an underestimated source of carbon and H_2 to the ocean.

Methods
Sampling and general fluid properties
Hydrothermal vent fluids were sampled using isobaric gas-tight (IGT) hydrothermal fluid samplers[53] attached to the ROV MARUM-QUEST 4000 (Supplementary Fig. S2). The samplers are made of inert titanium and provide real time temperature measurements during sample intake. After recovery of hydrothermal fluids pressure in the sampler is maintained during subsampling in the laboratory, which allows for genuine analysis of dissolved gases in aliquots drawn from the sampler.

Fluid samples were processed immediately after dives, typically within few hours after the sampling procedure at the seafloor. After subsamples for gas analytics were drawn from the IGTs conductivity, Eh and pH values were determined using a Multi-parameter portable meter (WTW MultiLine® Multi 3630 IDS®) equipped with a SenTix® 940 pH electrode, a SenTix®ORP-T 900 Eh sensor and a TetraCon® 925 conductivity measurement cell.

All measurements were conducted at laboratory temperatures around 21 °C. Aliquots for various ship- and shore-based analyses were prepared. These preparations included extraction of volatiles via headspace extraction (gas chromatography), filtration through 0.2 μm polyethylensulfon (PES)

filters under a laminar flow bench (IC; Ion Chromatography), filtration and acidification to pH < 2, using suprapure HCl and storage in acid cleaned LDPE bottles (ICP-OES; Inductively Coupled Plasma Optical Emission Spectroscopy). Cold storage at 4 °C was applied to sample aliquots for IC, ICP-OES and Photometry and untreated sample aliquots were frozen at −24 °C for nutrient analysis.

ICP-OES and IC
Major anions (Cl⁻, SO₄²⁻, Br⁻) were determined on 150-fold diluted sample aliquots at Constructor University Bremen using a Metrohm 761 Compact IC system equipped with a Metrosep A Supp 5-150/4.0 column. As eluent a mixture of sodium carbonate (Na_2CO_3) and sodium bicarbonate ($NaHCO_3$) in deionized water, with a final concentrations of 1.0 mM Na_2CO_3 and 3.2 mM $NaHCO_3$ was used. Precision and accuracy were assessed by analysis of IAPSO as a standard seawater reference material, with an analytical uncertainty for the above mentioned anions of below 2%. Analysis of major elements (Na, K, Mg, Ca, Si, Sr) were carried out at the MARUM Sediment Geochemistry Lab, University of Bremen by ICP-OES on a Varian Vista Pro (equipped with an argon gas humidifier, a seaspray nebulizer and a cyclonic spray chamber). Samples were measured in 20-fold dilution. The machine was calibrated with a sample adapted mix of lab single element standards in 5 concentration levels. Data quality was assessed by measurements of IAPSO P-series (recommended values for major and minor elements and supplied by Ocean Scientific International Ltd), which is standardized real seawater with a salintiy of 34.994 psu. External precision for IAPSO was better than 5.5% and external accuracy is better than 1.5%. Internal precision was better than 3%. Due to the necessary dilution for sample measurements, detection limits for less abundant elements were as follows: Al (3.7 μM), Ba (0.3 μM), Cu (1.6 μM), Fe (0.7 μM), Li (28.8 μM), Mn (0.4 μM), and P (32.3 μM), with similar internal precision better than 3%.

Sulfide & nutrients measurement
Immediately after the samples have been drawn from the IGT sampler, aliquots of 100 and 750 μL were given into 1.8 and 4.0 mL glass vials,

Fig. 5 | Predicted concentrations of selected chemical species for a reaction-path model in which preheated and prereacted seawater reacts with organic matter-bearing sediment at 400 °C and 500 bar. The initial SO_4-poor fluid was generated by reacting seawater with the same (but organic matter-free) sediment at 200 °C and a water-rock ratio of 10. Note that the change in slope of CH_4 and CO_2 at high water-rock ratios (W/R > 10) results from consumption of CH_4 and production of CO_2 and H_2 via the Sabbatier reaction (Reaction 1). The predicted alteration mineral assemblages corresponding to this reaction path are provided in Supplementary Fig. S11.
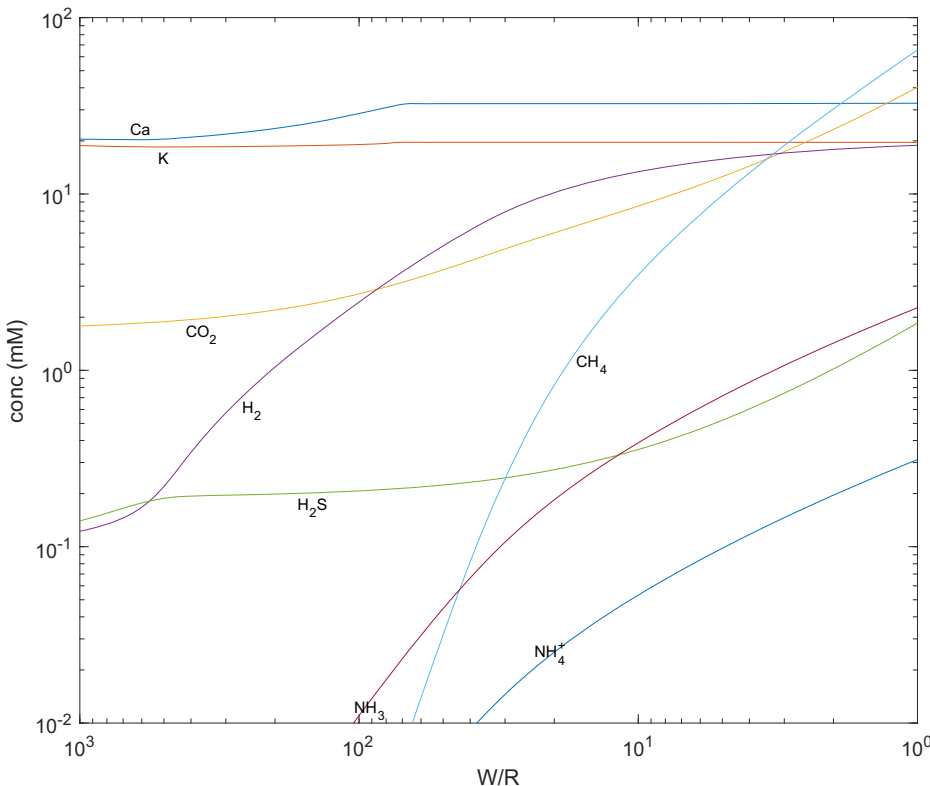
which were pre-filled with 11.8 mM and 47.4 mM of zinc acetate solution. The zinc acetate solution was prepared on a weekly basis by sparging ultrapure water with N_2 gas for 15 min to remove oxygen prior to dissolving zinc acetate. The samples were measured photometrically using the methylene blue method[79]. The photometric measurements were performed at the MARUM Sediment Geochemistry Lab, University of Bremen.

Nutrients (ammonium, nitrate and phosphate) and total alkalinity were measured at the Leibniz Center for Tropical Marine Research. A Tecan infinite M 200pro microplate spectrophotometer from TECAN Trading AG (Switzerland) was used. The methods presented by Benesch and Mangelsdorf[80], Sarazin, et al.[81]. and Ringuet, et al.[82]. were adapted to improve the resolution at low concentrations. For all parameters despite ammonium precision and accuracy have been controlled using either reference materials RMNS, KANSO or Dickson. In both cases the accuracy was better than 2%, except of phosphate where it was better than 6.3%. The precision for all parameters was better than 1%.

Analyses of dissolved gases
Dissolved gases were measured by an improved and modified method derived from Reeves, et al.[83]. For this, dissolved gases were first extracted from the liquid samples via headspace extraction before they were inserted in a custom-made sample injection system and determined via gas chromatography using an Agilent 7820 A gas chromatograph operated at 70 °C. Nitrogen was used as carrier gas and the compounds were separated by a Molsieve 60/80 column (Sigma-Aldrich, St Louis, MO) before they were determined via a thermal conductivity detector (H_2) and a flame ionization detector (CH_4). The system was calibrated with a certified reference gas mixture (Air Liquide, Crystal) with 0.999 mol-% H_2 and 1.014 mol-% CH_4 in a matrix of N_2. The reproducibility during the calibration in all cases was better than 1% relative. All samples were measured in triplicates from individual fluid aliquots. The reproducibility was 4% relative or significantly better for all samples.

Total dissolved CO_2 was determined by gas chromatography in the Laboratory Petrology of the Oceancrust at the University Bremen. Samples were stored in evacuated He-filled glass vials. The aliquots were acidified with 25 wt.% phosphoric acid to convert all DIC species to CO_2. The samples were measured with a Thermo Scientific Trace GC Ultra equipped with a Haysep 80/100 column (Sigma-Aldrich, St Louis, MO) using He as carrier gas at 50 °C. The CO_2 concentration was detected with a TCD detector. The system was calibrated with a certified reference gas mixture of CO_2 in a He matrix. The measurement was validated using a control standard solution with 25 mM CO_2. Two control standards measured in triplicates resulted in an average value of 22.8 mM suggesting accuracy was better than 10%. All measurements in triplicates yielded a reproducibility of better than 3%.

Analysis of light hydrocarbons and stable hydrogen and carbon isotopes analyses
Volatiles were extracted from IGT samples by a headspace extraction and transferred into 20 mL glass vials prefilled with satured NaCl solution for storage. Molecular compositions of light hydrocarbons (C_1 to C_6) were analyzed onboard with a 7890B (Agilent Technologies) gas chromatograph equipped with a HP-PLOT/Q capillary column and a flame ionization detector. Calibrations and performance checks of the analytical system were conducted regularly using commercial pure gas standards and gas mixtures. The coefficient of variation determined for the analytical procedure is lower than 2%. The molecular hydrocarbon composition is expressed as $C_1/(C_2–C_3)$.

Stable carbon and hydrogen isotope ratios ($^{13}C/^{12}C$ and $^2H/^1H$) of CO_2, CH_4 and H_2 were determined by gas chromatography-compound specific isotope ratio mass spectrometry in the MARUM Stable Isotope Laboratory as described in Pape, et al.[84]. For this, a Trace GC Ultra-GC IsoLink connected to a MAT 253 isotope ratio mass spectrometer via a ConFlo IV interface (all components Thermo Fisher Scientific Inc.) was used. Reported isotope ratios are arithmetic means (of duplicate measurements at least) in the δ-notation relative to Vienna Pee Dee Belemnite (VPDB) and Vienna Standard Mean Ocean Water (VSMOW) for carbon and hydrogen, respectively. Reproducibility was checked daily using commercial CH_4 standards (Isometric Instruments, Canada; Air Liquide GmbH, Germany).

Article

Standard deviations of triplicate stable isotope measurements were <0.5‰ for $\delta^{13}C$-CO_2 and $\delta^{13}C$-CH_4 and <1.0‰ for δ^2H-CH_4 and δ^2H-H_2.

Stable hydrogen and oxygen isotope ratios (δ^2H-H_2O, $\delta^{18}O$-H_2O) in water were measured using cavity ringdown spectroscopy (DLT-100 – Los Gatos Research, USA) in the Geochemistry and Hydrogeology group's laboratories at the Department of Geosciences, University Bremen. Lead by 6 equilibrating injections, each sample was measured in quadruples and analysis were averaged with the standard deviation falling well within the range recommended by the IAEA ($\delta^2H < 2$‰, $\delta^{18}O < 0.3$‰, Aggarwal, et al.[85]). Analyses were calibrated with externally referenced in-house standards bracketing the sample blocks. Accuracy was monitored through repeated measurements of the VSMOW standard ($n = 3$) with a maximum deviation of 2.27‰ (δ^2H) and 0.38‰ ($\delta^{18}O$).

X-ray fluorenscence analysis of bulk rock samples
Whole rock X-Ray Fluorescence (XRF) analyses of major- and trace elements were conducted at the University of Oldenburg on a Panalytical AXIOSmax wavelength dispersive X-Ray Fluorescence Spectrometer. Representative rock fragments were ground to powder and fused to glass tablets. International standard materials (SDO-1 and BE-N, Govindaraju[86]) were measured to monitor analytical accuracy, which is <3% for major elements and <5% for selected trace elements for BE-N. Accuracy for SDO-1 is worse but generally below 8% except for MnO (14.1%), P_2O_5 (9.1%) and Ni (11.6%).

Computational methods
Isotope equilibrium temperatures for $\delta^{13}C$ were calculated using isotope fractionation factors after Horita[62] (Eq. 2). δ^2H isotope equilibrium temperatures for the systems H_2-H_2O (Eq 3) and H_2-CH_4 (Eq. 4) were calculated using isotope fractionation factors after Horibe and Craig[87].

$$10^3 \ln\alpha(CO_2 - CH_4) = 26.70 - -49.137 * (10^3/T) + 40.828 * (10^6/T) - -7.512(10^9/T) \tag{2}$$

$$\alpha(H_2O - H_2) = 1.0473 + 201036/T^2 + 2.060 * 10^9/T^4 + 0.180 * 10^{15}/T^6 \tag{3}$$

$$\alpha(CH_4 - H_2) = 0.8994 + 183.54/T^2 \tag{4}$$

Quartz solubility was calculated for the chemical system H_2O-CO_2-CH_4-$NaCl$-KCl using the software package LonerAP (developed by R.J. Bakker 2008, Fluid Inclusion Laboratory Leoben), which uses the approaches of Akinfiev and Diamond[88] and Manning[89]. Saturation was calculated for different temperatures and pressures for a fluid with concentrations of 460 mM NaCl, 20 mM KCl, 60 mM CH_4 and 40 mM CO_2 that closely resemble the vent fluid composition.

Vapor brine equilibria were calculated for the chemical system H_2O-$NaCl$ according to empirical solution of Driesner and Heinrich[90]. The software SOWAT (sowatflinc_plotdata, version 0.1/2007) was used to calculate isobaric sections of the V + L plane. From these isobaric sections the intersection of a 3.1 wt.% NaCl equivalent fluid was interpolated to provide p-T conditions for a phase separating fluid in vapor-brine equilibrium.

Thermodynamic equilibrium calculations were performed with the SUPCRT92 software package[91]. The database used for this study combines all upgrades from the "slop98.dat" and the "speq02.dat" databases by Wolery and Jove-Colon[92] and data for heazlewoodite and pentlandite from Klein and Bach[61]. Temperature dependend Log K values were calculated for the Sabbatier reaction (Eq. 1), the pyrrhotite-pyrite buffer (Eq. 5) and the pentlandite-pyrrhotite-heazlewoodite buffer (Eq. 6) at 350 bar.

$$FeS + H_2S \rightleftharpoons FeS_2 + H_2 \tag{5}$$

$$2Fe_{4.5}Ni_{4.5}S_8 + H_2 \rightleftharpoons 9FeS + 3Ni_3S_2 + H_2S \tag{6}$$
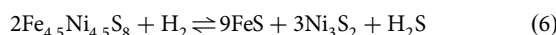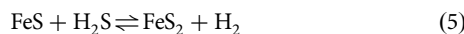
Reaction path models were conducted using the software Geochemist Workbench[93]. The Debye-Huckel activity model and a Taylor-made (SUPCRT92) thermodynamic database for 500 bar was used. In a first step seawater was heated to 200 °C and reacted with C_{org}-free sediment at a water to rock ratio of 10. Mineral precipitation was allowed for this pre-react procedure that simulates reaction of the hydrothermal fluid during the fluid recharge before reaching the high-temperature reaction-zone. The seawater was then heated to 400 °C with all minerals suppressed to simulate rapid heating in the vicinity of the reaction-zone. The 400 °C hot fluid was subsequently reacted with the same sediment including 0.22 wt.% of organic matter till a water-rock ratio of one was reached. The components used during the reaction path model and the resulting reaction-zone fluid are tabulated in Supplementary Table S10 the equilibrium mineral assemblages are shown in Supplementary Fig. S11.

Reporting summary
Further information on research design is available in the Nature Portfolio Reporting Summary linked to this article.

Data availability
Hydrothermal vent fluid data produced in this study is tabulated in the article and provided in the supplementary materials. Hydrothermal vent fluid data used for comparison is available at the data center PANGAEA under Creative Commons Attribution 4.0 International (https://doi.org/10.1594/PANGAEA.972999). All remaining methods and data are made available in the methods section and in the supplementary information.

References
1. Beaulieu, S. E., Baker, E. T. & German, C. R. Where are the undiscovered hydrothermal vents on oceanic spreading ridges? *Deep Sea Res. Part II: Topical Stud. Oceanogr.* **121**, 202–212 (2015).
2. Von Damm, K. L., Edmond, J. M., Grant, B. & Measures, C. I. Chemistry of submarine hydrothermal solutions at 21°N, East Pacific Rise. *Geochim. Et. Cosmochim. Acta* **49**, 2197–2220 (1985).
3. Butterfield, D. A., Massoth, G. J., McDuff, R. E., Lupton, J. E. & Lilley, M. D. Geochemistry of hydrothermal fluids from Axial Seamount hydrothermal emissions study vent field, Juan de Fuca Ridge: subseafloor boiling and subsequent fluid-rock interaction. *J. Geophys. Res.* **95**. https://doi.org/10.1029/JB095iB08p12895 (1990).
4. Gamo, T. et al. Chemical characteristics of hydrothermal fluids from the TAG Mound of the Mid-Atlantic Ridge in August 1994: Implications for spatial and temporal variability of hydrothermal activity. *Geophys. Res. Lett.* **23**, 3483–3486 (1996).
5. Von Damm, K. L., Bray, A. M., Buttermore, L. G. & Oosting, S. E. The geochemical controls on vent fluids from the Lucky Strike vent field, Mid-Atlantic Ridge. *Earth Planet. Sci. Lett.* **160**, 521–536 (1998).
6. Bowers, T. S. et al. Chemical controls on the composition of vent fluids at 13°-11°N and 21°N, East Pacific Rise. *J. Geophys. Res. Solid Earth* **93**, 4522–4536 (1988).
7. Syverson, D. D., Awolayo, A. N. & Tutolo, B. M. Seafloor spreading and the delivery of sulfur and metals to Earth's oceans. *Geology*. https://doi.org/10.1130/g51311.1 (2023).
8. Von Damm, K. L. et al. Extraordinary phase separation and segregation in vent fluids from the southern East Pacific Rise. *Earth Planet. Sci. Lett.* **206**, 365–378 (2003).
9. Von Damm, K. L. et al. Direct observation of the evolution of a seafloor 'black smoker' from vapor to brine. *Earth Planet. Sci. Lett.* **149**, 101–111 (1997).
10. Früh-Green, G. L. et al. Diversity of magmatism, hydrothermal processes and microbial interactions at mid-ocean ridges. *Nat. Rev. Earth Environ.* **3**, 852–871 (2022).

11. Cannat, M. Emplacement of mantle rocks in the seafloor at mid-ocean ridges. *J. Geophys. Res. Solid Earth* **98**, 4163–4172 (1993).

12. Nakamura, K. et al. Serpentinized troctolites exposed near the Kairei Hydrothermal Field, Central Indian Ridge: Insights into the origin of the Kairei hydrothermal fluid supporting a unique microbial ecosystem. *Earth Planet. Sci. Lett.* **280**, 128–136 (2009).

13. Gallant, R. M. & Von Damm, K. L. Geochemical controls on hydrothermal fluids from the Kairei and Edmond Vent Fields, 23°-25°S, Central Indian Ridge. *Geochem. Geophys. Geosyst.* **7**, n/a-n/a. https://doi.org/10.1029/2005gc001067 (2006).

14. Seyfried, W. E., Pester, N. J., Tutolo, B. M. & Ding, K. The Lost City hydrothermal system: constraints imposed by vent fluid chemistry and reaction path models on subseafloor heat and mass transfer processes. *Geochim. et. Cosmochim. Acta* **163**, 59–79 (2015).

15. Aquino, K. A. et al. Multi-stage evolution of the Lost City hydrothermal vent fluids. *Geochim. et. Cosmochim. Acta* **332**, 239–262 (2022).

16. Charlou, J. L., Donval, J. P., Fouquet, Y., Jean-Baptiste, P. & Holm, N. Geochemistry of high H_2 and CH_4 vent fluids issuing from ultramafic rocks at the Rainbow hydrothermal field (36°14′N, MAR). *Chem. Geol.* **191**, 345–359 (2002).

17. Schmidt, K., Koschinsky, A., Garbe-Schönberg, D., de Carvalho, L. M. & Seifert, R. Geochemistry of hydrothermal fluids from the ultramafic-hosted Logatchev hydrothermal field, 15°N on the Mid-Atlantic Ridge: Temporal and spatial investigation. *Chem. Geol.* **242**, 1–21 (2007).

18. Ishibashi, J.-I. et al. Diversity of fluid geochemistry affected by processes during fluid upwelling in active hydrothermal fields in the Izena Hole, the middle Okinawa Trough back-arc basin. *Geochem. J.* **48**, 357–369 (2014).

19. Seewald, J. S. et al. Spatial evolution and temporal stability of hydrothermal processes at sediment-covered spreading centers: constraints from Guaymas Basin, Gulf of California. *Geochim. et. Cosmochim. Acta* **367**, 87–106 (2024).

20. Toki, T. et al. Sr isotopic ratios of hydrothermal fluids from the Okinawa Trough and the implications of variation in fluid–sediment interactions. *Prog. Earth Planet. Sci.* **9**. https://doi.org/10.1186/s40645-022-00519-x (2022).

21. Ishibashi, J. et al. Helium and carbon geochemistry of hydrothermal fluids from the Mid-Okinawa Trough Back-Arc Basin, Southwest of Japan. *Chem. Geol.* **123**, 1–15 (1995).

22. Sakai, H. et al. Unique chemistry of the hydrothermal solution in the Mid-Okinawa Trough Backarc Basin. *Geophys. Res. Lett.* **17**, 2133–2136 (1990).

23. Kawagucci, S. et al. Hydrothermal fluid geochemistry at the Iheya North field in the mid-Okinawa Trough: Implication for origin of methane in subseafloor fluid circulation systems. *Geochem. J.* **45**, 109–124 (2011).

24. Kawagucci, S. et al. Geochemical origin of hydrothermal fluid methane in sediment-associated fields and its relevance to the geographical distribution of whole hydrothermal circulation. *Chem. Geol.* **339**, 213–225 (2013).

25. Cruse, A. M. & Seewald, J. S. Geochemistry of low-molecular weight hydrocarbons in hydrothermal fluids from Middle Valley, northern Juan de Fuca Ridge. *Geochim. et. Cosmochim. Acta* **70**, 2073–2092 (2006).

26. Von Damm, K. L., Edmond, J. M., Measures, C. I. & Grant, B. Chemistry of submarine hydrothermal solutions at Guaymas Basin, Gulf of California. *Geochim. et. Cosmochim. Acta* **49**, 2221–2237 (1985).

27. Campbell, A. C., German, C. R., Palmer, M. R., Gamo, T. & Edmond, J. M. Chemistry of hydrothermal fluids from Escabana Trough, Gorda Ridge in *Geologic, Hydrothermal and Biologic Studies at Escabana Through, Gorda Ridge, Offshore Northern Carolina*. Vol. U.S. Geological Survey Bulletin 2022 (eds J. L. Morton, R. A. Zierenberg, & C. A. Reiss) Ch. 11, 201-221 (Goverment Publishing Office, 1994).https://doi.org/10.3133/b2022

28. Baumberger, T. et al. Fluid composition of the sediment-influenced Loki's Castle vent field at the ultra-slow spreading Arctic Mid-Ocean Ridge. *Geochim. et. Cosmochim. Acta* **187**, 156–178 (2016).

29. Gamo, T., Sakai, H., Kim, E. S., Shitashima, K. & Ishibashi, J. High alkalinity due to sulfate reduction in the CLAM hydrothermal field, Okinawa Trough. *Earth Planet. Sci. Lett.* **107**, 328–338 (1991).

30. Pedersen, R. B., Thorseth, I. H., Nygård, T. E., Lilley, M. D. & Kelley, D. S. Hydrothermal activity at the Arctic mid-ocean ridges in *Diversity of Hydrothermal Systems on Slow Spreading Ocean Ridges. Geophysical Monograph Series* 67-89 https://doi.org/10.1029/2008gm000783 (2010).

31. Dumais, M. A., Gernigon, L., Olesen, O., Johansen, S. E. & Brönner, M. New interpretation of the spreading evolution of the Knipovich Ridge derived from aeromagnetic data. *Geophys. J. Int.* **224**, 1422–1428 (2021).

32. Engen, Ø, Faleide, J. I. & Dyreng, T. K. Opening of the Fram Strait gateway: a review of plate tectonic constraints. *Tectonophysics* **450**, 51–69 (2008).

33. Curewitz, D. et al. Structural analysis of fault populations along the oblique, ultra-slow spreading Knipovich Ridge, North Atlantic Ocean, 74°30′N-77°50′N. *J. Struct. Geol.* **32**, 727–740 (2010).

34. Schlindwein, V., Demuth, A., Korger, E., Läderach, C. & Schmid, F. Seismicity of the Arctic mid-ocean Ridge system. *Polar Sci.* **9**, 146–157 (2015).

35. Meier, M. et al. Segment-Scale Seismicity of the Ultraslow Spreading Knipovich Ridge. *Geochem. Geophys. Geosyst.* **22**. https://doi.org/10.1029/2020gc009375 (2021).

36. Meier, M., Schlindwein, V. & Schmid, F. Magmatic activity and dynamics of melt supply of volcanic centers of ultraslow spreading ridges: hints from local earthquake tomography at the Knipovich Ridge. *Geochem. Geophys. Geosyst.* **23**. https://doi.org/10.1029/2021gc010210 (2022).

37. Kokhan, A. V., Dubinin, E. P., Grokholsky, A. L. & Abramova, A. S. Kinematics and characteristic features of the morphostructural segmentation of the Knipovich Ridge. *Oceanology* **52**, 688–699 (2012).

38. Bohrmann, G. et al. Hydrothermal Systems Along Knipovich Ridge, Cruise No. MSM109, 6 July - 3 August 2022, Tromsø (Norway) - Reykjavik (Iceland) *MERIAN-Berichte* https://doi.org/10.48433/cr_msm109 (2022).

39. Sokolov, S. Y., Abramova, A. S., Zaraiskaya, Y. A., Mazarovich, A. O. & Dobrolyubova, K. O. Recent tectonics in the northern part of the Knipovich Ridge, Atlantic ocean. *Geotectonics* **48**, 175–187 (2014).

40. Roerdink, D. L. et al. Hydrothermal activity fuels microbial sulfate reduction in deep and distal marine settings along the Arctic Mid Ocean Ridges. *Front. Mar. Sci.* **10**. https://doi.org/10.3389/fmars.2023.1320655 (2024).

41. Krajewska, M., Lubecki, L. & Szymczak-Żyła, M. Sources of sedimentary organic matter in Arctic fjords: Evidence from lipid molecular markers. *Continental Shelf Res.* **264**. https://doi.org/10.1016/j.csr.2023.105053 (2023).

42. Hughes, A. L. C., Gyllencreutz, R., Lohne, ØS., Mangerud, J. & Svendsen, J. I. The last Eurasian ice sheets – a chronological database and time-slice reconstruction, DATED-1. *Boreas* **45**, 1–45 (2015).

43. Knies, J. et al. Arctic fjord ecosystem adaptation to cryosphere meltdown over the past 14,000 years. *Commun. Earth Environ.* **6**. https://doi.org/10.1038/s43247-025-02251-y (2025).

44. Ślubowska-Woldengen, M. et al. Advection of Atlantic Water to the western and northern Svalbard shelf since 17,500calyr BP. *Quat. Sci. Rev.* **26**, 463–478 (2007).

45. Bohrmann, G. et al. The Jøtul hydrothermal field - Magma-sediment interaction at the ultraslow-spreading Knipovich Ridge, Cruise No. MSM131, 18 August - 28 September 2024, Reykjavik (Iceland) - Emden (Germany). *MARIA S. MERIAN-Berichte* **MSM131**, 1-102. https://doi.org/10.48433/cr_msm131 (2025).

46. Bohrmann, G. et al. Discovery of the first hydrothermal field along the 500-km-long Knipovich Ridge offshore Svalbard (the Jøtul field). *Sci. Rep.* **14**, 10168 (2024).

47. Escartín, J. et al. Tectonic structure, evolution, and the nature of oceanic core complexes and their detachment fault zones (13°20′N and 13°30′N, Mid Atlantic Ridge). *Geochem. Geophys. Geosyst.* **18**, 1451–1482 (2017).

48. Blackman, D. K. et al. Geology of the Atlantis Massif (Mid-Atlantic Ridge, 30 degrees N): Implications for the evolution of an ultramafic oceanic core complex. *Mar. Geophys. Res.* **23**, 443–469 (2002).

49. Smith, D. K., Cann, J. R. & Escartin, J. Widespread active detachment faulting and core complex formation near 13 degrees N on the Mid-Atlantic Ridge. *Nature* **442**, 440–443 (2006).

50. Tucholke, B. E., Behn, M. D., Buck, W. R. & Lin, J. Role of melt supply in oceanic detachment faulting and formation of megamullions. *Geology* **36**. https://doi.org/10.1130/g24639a.1 (2008).

51. Buck, W. R., Lavier, L. L. & Poliakov, A. N. B. Modes of faulting at mid-ocean ridges. *Nature* **434**, 719–723 (2005).

52. Mezri, L. et al. Tectonic controls on melt production and crustal architecture during magma-poor seafloor spreading. *Earth Planet. Sci. Lett.* **628**. https://doi.org/10.1016/j.epsl.2024.118569 (2024).

53. Seewald, J. S., Doherty, K. W., Hammar, T. R. & Liberatore, S. P. A new gas-tight isobaric sampler for hydrothermal fluids. *Deep Sea Res. Part I: Oceanogr. Res. Pap.* **49**, 189–196 (2002).

54. Seyfried, W. E. Experimental and theoretical constraints on hydrothermal alteration processes at mid-ocean ridges. *Annu. Rev. Earth Planet. Sci.* **15**, 317–335 (1987).

55. Driesner, T. The system H2O–NaCl. Part II: Correlations for molar volume, enthalpy, and isobaric heat capacity from 0 to 1000 °C, 1 to 5000 bar, and 0 to 1 XNaCl. *Geochim. et. Cosmochim. Acta* **71**, 4902–4919 (2007).

56. Piepgras, D. J. & Wasserburg, G. J. Strontium and neodymium isotopes in hot springs on the East Pacific Rise and Guaymas Basin. *Earth Planet. Sci. Lett.* **72**, 341–356 (1985).

57. Shanks, W. C., Böhlke, J. K. & Seal, R. R. Stable Isotopes in Mid-Ocean Ridge Hydrothermal Systems: Interactions Between Fluids, Minerals, and Organisms in *Seafloor Hydrothermal Systems: Physical, Chemical, Biological, and Geological Interactions. Geophysical Monograph Series* 194-221 https://doi.org/10.1029/GM091p0194 (1995).

58. Diehl, A. & Bach, W. MARHYS Database 4 https://doi.org/10.1594/PANGAEA.972999 (2024).

59. Diehl, A. & Bach, W. MARHYS (MARine HYdrothermal Solutions) Database: A Global Compilation of Marine Hydrothermal Vent Fluid, End Member, and Seawater Compositions. *Geochem. Geophys. Geosyst.* **21**. https://doi.org/10.1029/2020gc009385 (2020).

60. Seyfried Jr., W. E., Foustoukos, D. I. & Allen, D. E. Ultramafic-hosted hydrothermal systems at mid-ocean ridges: chemical and physical controls on pH, redox and carbon reduction reactions in *Mid-Ocean Ridges: Hydrothermal Interactions Between the Lithosphere and Oceans*. Vol. 148 *Geophysical Monograph Series* (eds C. R. German, J. Lin, & L. M. Parson) https://doi.org/10.1029/148GM11 (2004).

61. Klein, F. & Bach, W. Fe-Ni-Co-O-S phase relations in peridotite-seawater interactions. *J. Petrol.* **50**, 37–59 (2009).

62. Horita, J. Carbon isotope exchange in the system CO2-CH4 at elevated temperatures. *Geochim. et. Cosmochim. Acta* **65**, 1907–1919 (2001).

63. Giggenbach, W. F. Carbon-13 exchange between CO2 and CH4 under geothermal conditions. *Geochim. et. Cosmochim. Acta* **46**, 159–165 (1982).

64. Kiyosu, Y. & Roy Krouse, H. Carbon isotope effect during abiogenic oxidation of methane. *Earth Planet. Sci. Lett.* **95**, 302–306 (1989).

65. McCollom, T. M. Observational, experimental, and theoretical constraints on carbon cycling in mid-ocean ridge hydrothermal systems. in *Magma to Microbe: Modeling Hydrothermal Processes at Ocean Spreading Centers. Geophysical Monograph Series* 193-213 https://doi.org/10.1029/178gm10 (2008).

66. Arnórsson, S. & Gunnlaugsson, E. New gas geothermometers for geothermal exploration—calibration and application. *Geochim. et. Cosmochim. Acta* **49**, 1307–1325 (1985).

67. Welhan, J. A. Origins of methane in hydrothermal systems. *Chem. Geol.* **71**, 183–198 (1988).

68. Seewald, J. S., Seyfried, W. E. & Shanks, W. C. Variations in the chemical and stable-isotope composition of carbon and sulfur species during organic-rich sediment alteration - an experimental and theoretical-study of hydrothermal activity at Guaymas Basin, Gulf of California. *Geochim. Et. Cosmochim. Acta* **58**, 5065–5082 (1994).

69. Bischoff, J. L. & Rosenbauer, R. J. Erratum: The critical point and two-phase boundary of seawater, 200–500 °C. *Earth Planet. Sci. Lett.* **68**, 172–180 (1984).

70. Bickert, M., Cannat, M. & Brunelli, D. Hydrous fluids down to the semi-brittle root zone of detachment faults in nearly amagmatic ultra-slow spreading ridges. *Lithos* **442-443**. https://doi.org/10.1016/j.lithos.2023.107084 (2023).

71. Cannat, M. et al. On spreading modes and magma supply at slow and ultraslow mid-ocean ridges. *Earth Planet. Sci. Lett.* **519**, 223–233 (2019).

72. Dunn, R. A., Arai, R., Eason, D. E., Canales, J. P. & Sohn, R. A. Three-dimensional seismic structure of the mid-atlantic ridge: an investigation of tectonic, magmatic, and hydrothermal processes in the Rainbow Area. *J. Geophys. Res. Solid Earth* **122**, 9580–9602 (2017).

73. Zhao, M., Canales, J. P. & Sohn, R. A. Three-dimensional seismic structure of a Mid-Atlantic Ridge segment characterized by active detachment faulting (Trans-Atlantic Geotraverse, 25°55′N-26°20′N). *Geochem. Geophys. Geosyst.* **13**. https://doi.org/10.1029/2012gc004454 (2012).

74. Momoh, E., Cannat, M. & Leroy, S. Internal Structure of the Oceanic Lithosphere at a Melt-Starved Ultraslow-Spreading Mid-Ocean Ridge: Insights From 2-D Seismic Data. *Geochem. Geophys. Geosyst.* **21**. https://doi.org/10.1029/2019gc008540 (2020).

75. Gillis, K. M. & Coogan, L. A. A review of the geological constraints on the conductive boundary layer at the base of the hydrothermal system at mid-ocean ridges. *Geochem. Geophys. Geosyst.* **20**, 67–83 (2019).

76. Wilcock, W. S. D. & Delaney, J. R. Mid-ocean ridge sulfide deposits: Evidence for heat extraction from magma chambers or cracking fronts? *Earth Planet. Sci. Lett.* **145**, 49–64 (1996).

77. Seewald, J. S. Aqueous geochemistry of low molecular weight hydrocarbons at elevated temperatures and pressures: constraints from mineral buffered laboratory experiments. *Geochim. et. Cosmochim. Acta* **65**, 1641–1664 (2001).

78. Miyazaki, J. et al. WHATS-3: an improved flow-through multi-bottle fluid sampler for deep-sea geofluid research. *Front. Earth Sci.* **5**. https://doi.org/10.3389/feart.2017.00045 (2017).

79. Cline, J. D. Spectrophotometric Determination of Hydrogen Sulfide in Natural Waters. *Limnol. Oceanogr.* **14**, 454–458 (1969).

80. Benesch, R. & Mangelsdorf, P. Eine Methode zur colorimetrischen Bestimmung von Ammoniak in Meerwasser. *Helgoländer Wissenschaftliche Meeresuntersuchungen* **23**, 365–375 (1972).

81. Sarazin, G., Michard, G. & Prevot, F. A rapid and accurate spectroscopic method for alkalinity measurements in sea water samples. *Water Res.* **33**, 290–294 (1999).

82. Ringuet, S., Sassano, L. & Johnson, Z. I. A suite of microplate reader-based colorimetric methods to quantify ammonium, nitrate, orthophosphate and silicate concentrations for aquatic nutrient monitoring. *J. Environ. Monit.* **13**, 370–376 (2011).

83. Reeves, E. P. et al. Geochemistry of hydrothermal fluids from the PACMANUS, Northeast Pual and Vienna Woods hydrothermal fields, Manus Basin, Papua New Guinea. *Geochimica et Cosmochimica Acta* **75**, 1088–1123 (2011).

84. Pape, T. et al. Origin and Transformation of light hydrocarbons ascending at an active pockmark on Vestnesa Ridge, Arctic Ocean. *J. Geophys. Res. Solid Earth* **125**. https://doi.org/10.1029/2018jb016679 (2020).

85. Aggarwal, P. K. et al. Laser Spectroscopic Analysis of Liquid Water Samples for Stable Hydrogen and Oxygen Isotopes. p.49 (IAEA, Wien, Austria, 2009).

86. Govindaraju, K. 1994 Compilation Of Working Values And Sample Description For 383 Geostandards. *Geostand. Newsl.* **18**, 1–158 (1994).

87. Horibe, Y. & Craig, H. fractionation in the system methane-hydrogen-water. *Geochim. et. Cosmochim. Acta* **59**, 5209–5217 (1995).

88. Akinfiev, N. N. & Diamond, L. W. A simple predictive model of quartz solubility in water–salt–CO_2 systems at temperatures up to 1000 °C and pressures up to 1000MPa. *Geochim. et. Cosmochim. Acta* **73**, 1597–1608 (2009).

89. Manning, C. E. The solubility of quartz in H_2O in the lower crust and upper mantle. *Geochim. et. Cosmochim. Acta* **58**, 4831–4839 (1994).

90. Driesner, T. & Heinrich, C. A. The system H_2O–NaCl. Part I: Correlation formulae for phase relations in temperature–pressure–composition space from 0 to 1000 °C, 0 to 5000bar, and 0 to 1 X_{NaCl}. *Geochim. et. Cosmochim. Acta* **71**, 4880–4901 (2007).

91. Johnson, J. W., Oelkers, E. H. & Helgeson, H. C. SUPCRT92: A software package for calculating the standard molal thermodynamic properties of minerals, gases, aqueous species, and reactions from 1 to 5000 bar and 0 to 1000 °C. *Comput. Geosci.* **18**, 899–947 (1992).

92. Wolery, T. & Jove-Colon, C. Qualification of thermodynamic data for geochemical modeling of mineral-water interactions in dilute systems. (Yucca Mountain Project, Las Vegas, Nevada, 2004).

93. Manning, D. Bethke, C. M. Geochemical and biogeochemical reaction modeling second Edition, 2007: Cambridge University Press, Cambridge, UK. 564pp., ISBN 978 0 521 87554 7. *Mineral. Mag.* **72**, 996–997 (2008).

Acknowledgements

Author contributions

A.D. fluid sampling operation, sample processing, analytical work, data analyses, data interpretation, conceptualization and creation of original MS draft, lead MS editing and revisions, fund acquisition, E.A. analytical work, edited original MS. P.M. analytical work, edited original MS. T.P. analytical work, data analysis, data interpretation, edited original and revised MS. E.M. analytical work, edited original MS. M.R. analytical work, data analysis, edited original MS. L.M. data analysis, data interpretation, edited original and revised MS. W.B. data analyses, data interpretation, edited original and revised MS. D.M. analytical work, edited original MS. C.H. analytical work, edited original MS. A.R. data analysis, data interpretation, edited original MS. K.S. edited original and revised MS. S.S.P. edited original MS. Y.M. edited original MS. I.B.A. edited original MS. C.K. edited original MS. S.-M.K. edited original MS. G.B. led operations at sea, data interpretation, edited original MS, fund acquisition.

Funding

Competing interests

The authors declare no competing interests.

Additional information

Supplementary information The online version contains supplementary material available at https://doi.org/10.1038/s43247-025-02962-2.

Correspondence and requests for materials should be addressed to Alexander Diehl.

Peer review information *Communications Earth & Environment* thanks the anonymous reviewers for their contribution to the peer review of this work. Primary Handling Editors: Renbiao Tao and Alireza Bahadori. A peer review file is available.

Reprints and permissions information is available at http://www.nature.com/reprints

Publisher's note Springer Nature remains neutral with regard to jurisdictional claims in published maps and institutional affiliations.